A revised manuscript to ***Environmental Science & Technology***

Persulfate activation on crystallographic manganese oxides: Mechanism of singlet oxygen evolution for nonradical selective degradation of aqueous contaminants

Shishu Zhu, [†,‡] Xiaojie Li, [†] Jian Kang, [†] Xiaoguang Duan,[*, §] and Shaobin Wang *[*, †, §]*

[†] Department of Chemical Engineering, Curtin University, GPO Box U1987, Perth, WA 6845, Australia

[‡] State Key Laboratory of Urban Water Resource and Environment, Harbin Institute of Technology, 73 Huanghe Road, Harbin 150090, P. R. China

[§] School of Chemical Engineering, The University of Adelaide, Adelaide, SA 5005, Australia

*Corresponding Authors:

xiaoguang.duan@adelaide.edu.au (X.D.); Phone: +61 8 8313 5447.

shaobin.wang@adelaide.edu.au (S.W.); Phone: +61 8 8313 3810.

ABSTRACT

Minerals and transitional metal oxides of earth-abundant elements are desirable catalysts for *in situ* chemical oxidation in environmental remediation. However, catalytic activation of peroxydisulfate (PDS) by manganese oxides was barely investigated. In this study, one-dimension manganese dioxides (α- and β-MnO_2) were discovered as effective PDS activators among the diverse manganese oxides for selective degradation of organic contaminants. Compared with other chemical states and crystallographic structures of manganese oxide, β-MnO_2 nanorods exhibited the highest phenol degradation rate (0.044 min^{-1}, 180 min) by activating PDS. A comprehensive study was conducted utilizing electron paramagnetic resonance, chemical probes, radical scavengers, and different solvents to identity the reactive oxygen species (ROS). Singlet oxygen ($^1O_2$) was unveiled to be the primary ROS, which was generated by direct oxidation or recombination of superoxide ions and radicals from a metastable manganese intermediate at neutral pH. The study dedicates to the first mechanistic study into PDS activation over manganese oxides and provides a novel catalytic system for selective removal of organic contaminants in wastewater.

INTRODUCTION

In situ chemical oxidation (ISCO) has been extensively applied for remediation of organic contaminants in soil and groundwater, taking leverage of highly reactive oxygen species (ROS) released from diverse peroxides. Persulfate (also known as peroxydisulfate, PDS) is more favorable in ISCO compared to hydrogen peroxide (H_2O_2), ozone (O_3), and peroxymonosulfate (PMS) due to better chemical stability in transport and storage, lower cost and longer half-life for a profound efficiency. [1] However, PDS activation usually requires an intensive energy input via physical approaches (UV, heat, and sonication), which elevates the operational cost in actual remediation of contaminated water matrix. Dionysiou and co-workers discovered that transition metal ions can promote homogeneous PDS dissociation to evolve sulfate radicals ($SO_4^{\bullet-}$) for organic mineralization.[2, 3] Furthermore, the ubiquitous presence of minerals at the subsurface environment inspired the investigations into the reactions between PDS and transition metal oxides. Copper oxide was reported to activate PDS to form a surface metastable complex, which can oxidize chlorophenols via a nonradical pathway. [4] Fang and co-workers illustrated that iron oxides (Fe_3O_4) can catalyze PDS to produce sulfate radicals derived from generated superoxide ion radicals ($O_2^{\bullet-}$). [5] The vanadium oxides also exhibited a high activity for sulfate radical production via electron transfer between PDS and redox centers of V(III)/V(IV). [6]

Manganese oxides are low in biotoxicity and rich in natural stock. As a dominated component of minerals in soils or aquifer materials, manganese dioxide (MnO_2) with multivalent nature can either directly oxidize contaminants [7, 8] or catalyze hydrogen peroxide based ISCO. [9] Chemical probes and electron paramagnetic resonance (EPR) methods have confirmed that both $O_2^{\bullet-}$ and hydroperoxide (HO_2^-) were the dominated ROS in H_2O_2/MnO_2 at neutral pH. [9, 10] Our previous studies have illustrated

that crystalline MnO_2 can effectively activate PMS to generate $SO_4^{\bullet-}$ for phenol oxidation, and that the catalytic activity was intrinsically determined by the crystallographic structure, orientations, dimensions and nanostructures of manganese oxides. [11, 12] Nevertheless, PDS activation by manganese containing minerals was reported in early investigations, [13, 14] and the underlining mechanism has not yet been elucidated. Recently, the reactive complexes were discovered to be produced between PMS and amorphous MnO_2 interfaces as nonradical reactive species that can directly oxidize bisphenol-A. [15] Moreover, biogenic MnO_2 could activate PMS to produce singlet oxygen ($^1O_2$) via a self-decomposition and energy quenching mechanism. [16]

In this study, we performed a systematic investigation of PDS activation over a wide array of manganese oxides with different crystal structures and valence states. Intriguingly, one-dimensional MnO_2 was discovered to be most catalytically reactive to drive PDS decomposition to evolve singlet oxygen, rather than the aforementioned sulfate radical and nonradical pathways. Compared to free radicals ($SO_4^{\bullet-}$ 2.5–3.1 V vs. $^{\bullet}OH$ 2.7 V), the $^1O_2$-based system typically manifested a mild redox capacity (2.2 V) with a high selectivity to attack organic substrates. Since there are still debates on identification of $^1O_2$ in recent metal/metal-free advanced oxidation processes (AOPs), [17] we integrated several strategies to identify the ROS. Both chemical probes and *in situ* ROS capture by EPR suggested that $^1O_2$ was generated and accounted for the oxidation. The pH and solvent dependence further certified the dominated role of $^1O_2$, especially in neutral pH solution. A detailed mechanism was first proposed for PDS activation over manganese oxides to generate $^1O_2$. Therefore, this study may provide a new system for selective removal of targeted organic contaminants in water and boost the mechanistic innovations in PDS-based ISCO.

MATERIALS AND METHODS

Materials preparation and characterization. Firstly, different manganese dioxides (α-, β-, and γ-MnO_2) were synthesized from the previous studies. [11, 18, 19] Briefly, a certain amount of $(NH_4)_2S_2O_8$ was employed to react with $MnSO_4$ in a hydrothermal process. The different crystal structures of manganese dioxides were achieved by controlling the concentration of inorganic cations and reaction temperatures. Moreover, we prepared Mn_2O_3 and Mn_3O_4 under oxidation conditions. [20] The details of the preparation are provided in Supporting Information (SI, Text 1). The information of characterization instruments and their operation is also provided in SI, Text S2 and S6.

Catalytic performance evaluation. The degradation performance was evaluated in a batch reactor with organic compounds in a buffered solution. The oxidation was initiated by adding fixed amounts of catalyst and PDS at a rotation speed of 300 rpm. In evaluation of solution pH impacts, different buffers were adopted with 1 mM acetate for pH 5, 1 mM borate for pH 6.5 or 8.5, and 1 mM bicarbonate for pH 10. At certain time intervals, the solution was filtered through a 0.45 μm filter into a HPLC vial and mixed with methanol to terminate the oxidation. Benzoic acid (BA), nitrobenzene (NB), hydrobenzoic acid (HBA), bisphenol A (BPA), rhodamine B (RB), and phenol (PN) were chosen as probe contaminants to evaluate the oxidation capacity of PDS/manganese-oxide systems. The concentrations of the organic compounds were analyzed by an ultra-high performance liquid chromatography (UHPLC, Thermo Fisher, USA) with a C18 column. An UV–vis spectrophotometer (Spectronic 20 Genesys, Thermo Fisher, USA) was also used to determine Rhodamine B (RhB) concentration at the wavelength of 554 nm. The detailed analysis of organic compounds is provided in SI, Text 3. The PDS concentration was determined by a spectrophotometric method. [21] All the key

experiments were conducted in triplicates and presented with mean values and standard derivations in Figures.

Detection of ROS The radical scavengers of methanol (MeOH, 200-1000 mM), tert-butyl alcohol (TBA, 200 mM), sodium azide (NaN_3, 1 mM) and furfuryl alcohol (FFA, 0.1 - 1 mM) were added into β-MnO_2/PDS system to probe the generated ROS such as free radicals and singlet oxygen. Benzoquinone (BQ, 1 mM) and carbonate ion (CO_3^{2-}, 1 - 50 mM) were used to probe the superoxide intermediates. The solutions for radical quenching tests were buffered at pH of 6.5. The solvent effect of deuterated water (D_2O) and H_2O was investigated at constant buffered pH. An electron paramagnetic resonance (EPR) spectrometer (EMX 10/12, Bruker, Germany) was employed to detect the ROS by reacting with 5,5-dimethyl-1-pyrroline N-oxide (DMPO) and 2,2,6,6-tetramethyl-4-piperidinol (TEMP). The details of the methods and instrument parameters are listed in SI, Text S4 and S5. The photosensitized singlet oxygenation was adopted as a reference system to analyze the intermediate distribution and the details are provided in SI, Text S8.

RESULTS AND DISCUSSION

Persulfate activation on manganese oxides for catalytic degradation. Manganese oxides with different crystal structures and valence states were evaluated for PDS activation as shown in Figure 1. At neutrally buffered pH (6.5 ± 0.3), PDS alone cannot degrade PN (Figure S1) and adsorptive removal of PN on manganese oxides was very limited (Figure S2, < 12%). Over 99% PN removals were achieved in the presence of α-MnO_2 and β-MnO_2, which were apparently more reactive than other manganese oxides (γ-MnO_2, Mn_2O_3 and Mn_3O_4) with less than 30% PN degradation. Considering the moderate substrate concentration, the pseudo first-order kinetics was adopted. The corresponding rate

constants of manganese oxides were exhibited in Figure S1. The rate constants, k_1(PN), for β-MnO_2 and α-MnO_2 were 0.0441 min^{-1} and 0.0264 min^{-1}, respectively, which were higher than 0.0018 min^{-1} of γ-MnO_2. Manganese species in higher valence states were also evaluated showing lower values of k_1(PN) for Mn_2O_3 (0.0007 min^{-1}) and Mn_3O_4 (0.0001 min^{-1}).

Since Mn^{2+} ions are not reactive for catalytic PDS activation, [2] the impacts of Mn leaching can be ruled out. Thus, the discrepant catalytic performances of manganese oxides originate from the intrinsic properties of the chemical states and crystal orientations of manganese species. [11] The crystal structures of manganese oxides were identified by XRD patterns (Figure S3, Text S6). As illustrated in Figure S4, the crystallographic structures of α, β, and γ-MnO_2 were all built with edge-sharing MnO_6 octahedra. Distinctively, α-MnO_2 was composed of (2 × 2) and (1 × 1) tunnels. β-MnO_2 was provided with (1 × 1) tunnels while γ-MnO_2 was constructed with (2 × 2) and (1 × 2) tunnels. The (1 × 1) tunnel of MnO_2 has been reported to be beneficial for cleavage of peroxide bond whereas larger tunnels may restrain the catalytic potential. [22] This may explain the best PDS activation by α- and β-MnO_2. Moreover, manganese oxides with different oxidation states manifested different catalytic activities. Interestingly, Mn_2O_3 and Mn_3O_4 (Figures S1 and S2) with lower valence states (Mn^{2+}/Mn^{3+}) are not active, suggesting that the manganese species in PDS activation may not simply work as the electron donor as in Ag^+ [2] and zero-valent iron [23] based systems to evolve sulfate radicals. Then, β-MnO_2 was further investigated for the subsequent mechanistic and kinetic studies. The nanostructure of β-MnO_2 was spotted as nanorods with a width of 20 nm (Figures S5a, b and c) and specific surface area of 11.9 m^2/g (Figure S6). Uniform lattice fringes of 0.31 nm was identified in the HRTEM images (Figures S5d and e) representing for the [110] facet of β-MnO_2.

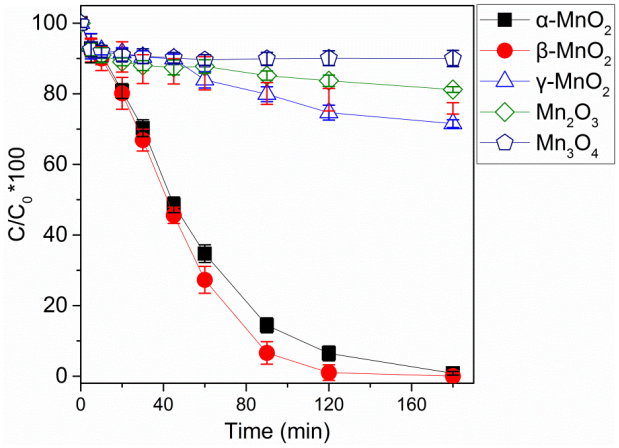

148

149 **Figure 1.** A comparison of PDS activation performances for phenol oxidative degradation by different
150 manganese oxides. [Manganese oxide]$_0$ = 400 mg/L, [PDS]$_0$ = 4 mM, [organics] = 100 μM, pH
151 buffered around 6.5.

152 The reactivity of β-MnO_2/PDS system toward different organic contaminants was also investigated.
153 BA was the chemical probe for $SO_4^{\bullet-}$ and $^{\bullet}OH$ (k_2 (BA, $SO_4^{\bullet-}$) = 1.2 ×10^9 M^{-1} s^{-1} and k_2 (BA, $^{\bullet}OH$) =
154 4.2 ×10^9 M^{-1} s^{-1}) [24], while NB was the chemical probe for $^{\bullet}OH$ (k_2 (NB, $^{\bullet}OH$) = 3.9 × 10^9 M^{-1} s^{-1})
155 accordingly. [25] In Figure 2a, BA and NB were barely oxidized (< 8%) in 180 min, indicating that both
156 $SO_4^{\bullet-}$ and $^{\bullet}OH$ were not generated in β-MnO_2/PDS. The complete oxidations of BPA, PN and RB and
157 a moderate removal efficiency of HBA (53.7%) were observed in Figure 2a. Similar selective oxidation
158 of organics was also observed in the nonradical pathways in previous studies. [26-28]

159 The ionization potential (IP) of the organic compounds has been utilized as an indicator to estimate
160 the redox capacity of an oxidative system. [29] In the electron mediation mechanism, an organic
161 compound with an IP beyond 9.0 eV (the threshold) cannot be oxidized in N-graphene/PMS system
162 due to the relatively mild redox potential of the surface confined metastable nonradical ROS. In this
163 work, BA and NB with IP values above the threshold were hardly decomposed (Figure 2b), whereas
164 the organics (PN, BPA, and HBA with lower IP values were vulnerable to be degraded with high

reaction rates (Table S1, Figures 2b and S7). This suggests that the oxidative system may not rely on free radicals but nonradical species. Some recent studies discovered that singlet oxygen ($^1O_2$) could be generated in non-photocatalytic AOPs, which also exhibited a high selectivity towards electron-rich phenolic compounds as the nonradical pathway. [30, 31] Therefore, the existence of $^1O_2$ in β-MnO_2/PDS system may need to be considered.

Probing the singlet oxygen generation in nonradical process. In order to confirm the contributions from free radicals during the oxidation, TBA and MeOH were employed to act as selective radical scavengers because of their distinct second-order rate constants with sulfate radicals (k_2(TBA, $SO_4^{\bullet-}$) = 4 - 9.5 × 10^5 M^{-1} s^{-1}, k_2(MeOH, $SO_4^{\bullet-}$) = 2.5 × 10^7 M^{-1} s^{-1}) and hydroxyl radicals (k_2(TBA, $^{\bullet}OH$) = 3.8 - 7.6 × 10^8 M^{-1} s^{-1}, k_2(MeOH, $^{\bullet}OH$) = 9.7 × 10^8 M^{-1} s^{-1}). [25, 32] The addition of 200 mM TBA or MeOH showed a negligible impact on phenol oxidation (Figure 3a), suggesting that both •OH and $SO_4^{\bullet-}$ were not produced. This can be confirmed by further increasing MeOH to 1000 mM which still cannot induce any adverse effect on phenol degradation (Figures 3a and S8).

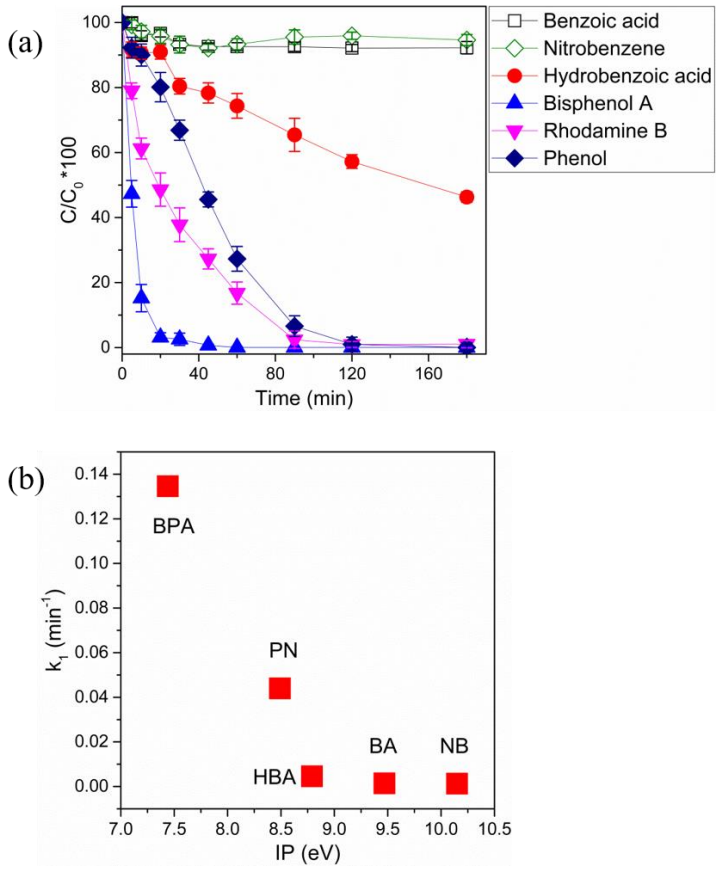

Figure 2. (a) Selective oxidation in β-MnO_2 /PDS activation. [Manganese oxide]$_0$ = 400 mg/L, [PDS]$_0$ = 4 mM, [organics] = 100 μM, pH buffered around 6.5. (b) The relationship between organics degradation rates and their ionization potentials (IP).

Moreover, we employed azide with a moderate concentration (1 mM) to quench the oxidation by $^1O_2$ (k_2 (NaN_3, $^1O_2$) = 1 × 10^9 M^{-1} s^{-1}). [33] In the presence of azide ions, phenol degradation by β-MnO_2/PDS was almost suspended (Figures 3b and S8) with only 12% removal in 180 min (mostly by adsorption, Figure S2). FFA was further used as a chemical probe for $^1O_2$ generation, which manifested a higher second order rate of 1.2 × 10^8 M^{-1} s^{-1} [34, 35] than the targeted phenolic compound (2.0-3.0 × 10^6 M^{-1} s^{-1}) [31, 36] with $^1O_2$. A minor amount of FFA (0.1 mM, equal to phenol concentration), caused a noticeable decline in phenol removal rate from 0.0441 to 0.0093 min^{-1} (Figures 3b and S8). When FFA was increased to 0.3 mM, the reaction rate further decreased to 0.0036 min^{-1} and phenol oxidation was

196 terminated with 1.0 mM FFA. Herein, both the selective radical quenching and chemical probing
197 indicated that $^1O_2$ was generated and accounted for the organic degradation in β-MnO_2/PDS system.
198 Notably, although azide and FFA also exhibited a high reactivity with free radicals (i.e. k_2 (NaN_3, $SO_4^{\bullet-}$)
199 = 2.5×10^9 M^{-1} s^{-1} and k_2 (FFA, $^{\bullet}OH$) = 1.5×10^{10} M^{-1} s^{-1}), [37, 38] the overabundant loading of MeOH
200 exhibited higher rates at 1 or 2 orders of magnitude towards the radicals. Since the inhibition effect of
201 MeOH was trivial, the sulfate and hydroxyl radicals were not produced and the reaction of azide or
202 FFA with the radicals could be neglected. Thus, azide and FFA could be regarded as the exclusive $^1O_2$
203 scavengers in the study. The quenching effects of TBA, MeOH, and FFA on phenol oxidation by α-
204 MnO_2/PDS (Figure S9) exhibited the similar characteristics to β-MnO_2, which implied the same
205 catalytic pathway involving $^1O_2$.

206 FFA decay was recorded to quantify the $^1O_2$ production in β-MnO_2/PDS system. In Figure 3c, PDS
207 alone cannot degrade FFA and FFA adsorption on β-MnO_2 was marginal. However, FFA began to
208 decompose once PDS and MnO_2 co-existed. At a low initial FFA concentration (0.1 mM), the
209 completed FFA oxidation was obtained within 60 min with a rate constant of 0.162 min^{-1}, which is
210 far higher than that of phenol (0.0441 min^{-1}). When the initial FFA concentration was increased to 0.3
211 mM and 1 mM, 99.5% and 39.2% of FFA degradations were observed, respectively. Assuming that
212 FFA decay follows a first order kinetics, then the values of $\ln([FFA]_t/[FFA]_0) = -k_{obs}\, t$, k_{obs} may be
213 relevant to [MnO_2], [PDS], and pH values. The correlation of $[FFA]_0$ and k_{obs} was fitted in Figure S10
214 and the good linear relationship (R^2 = 0.986) verified the first order kinetics of FFA degradation. The
215 first order rather than zero order kinetics indicated that the $^1O_2$ oxidation participated in the bulk
216 solution rather than on the catalyst surface region via electron transfer, which was also discovered in

previous $^1O_2$ based systems. [30, 39]

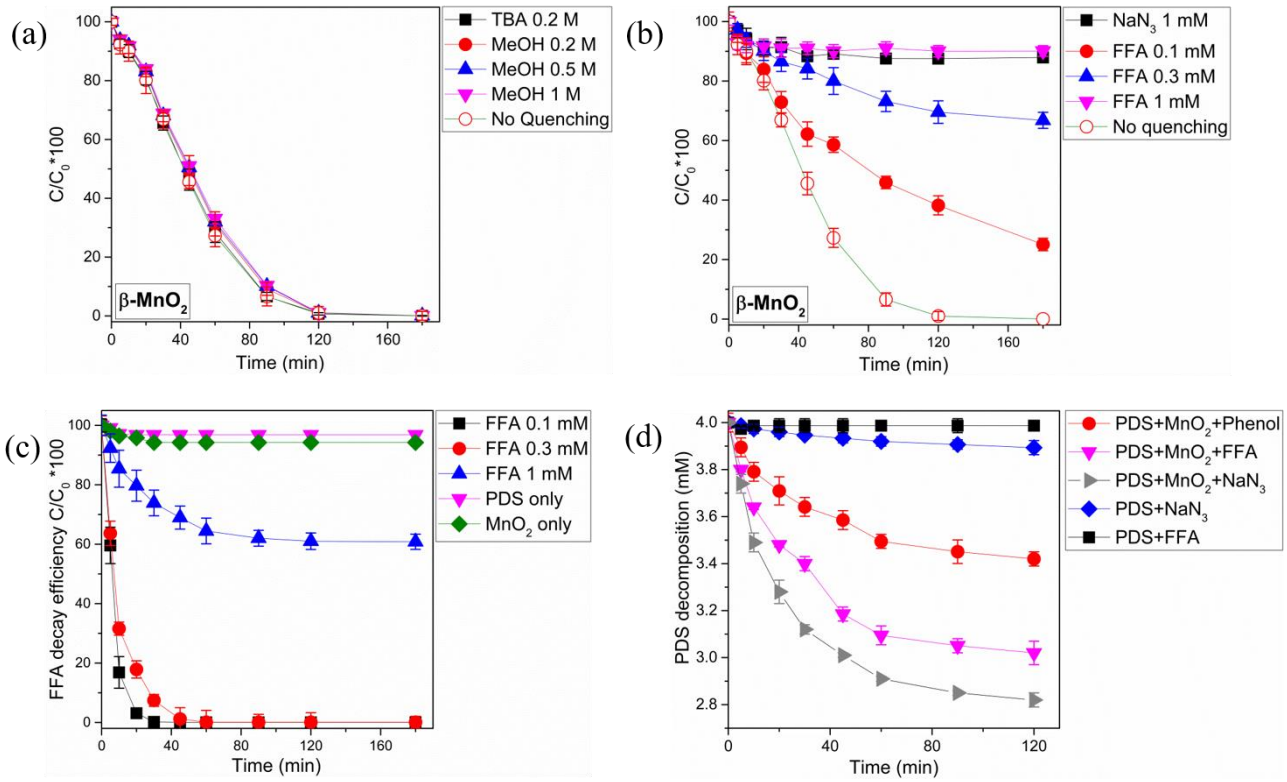

Figure 3. The determination of ROS species for oxidation in β-MnO_2/PDS. (a) the quenching effect of free radicals on phenol oxidation degradation (TBA 200 mM, MeOH 200-1000 mM), (b) the quenching effect of singlet oxygen on phenol oxidative degradation (NaN_3 1 mM, FFA 100-1000 μM), (c) FFA decay in β-MnO_2 /PDS (FFA conc. 100-1000 μM), (d) PDS decomposition under different experimental conditions (phenol or FFA conc. 100 μM). $[\beta\text{-}MnO_2]_0$ = 400 mg/L, $[PDS]_0$ = 4 mM, pH buffered around 6.5.

PDS concentration was monitored to affirm persulfate decomposition in different situations. PDS alone could not be consumed by phenol at neutral pH, whereas the presence of β-MnO_2 can decompose PDS to a certain extent without the presence of organics (Figure S11). The rapid PDS decomposition was not experienced in the study, which was different from the Ag^+/PDS system in continuously producing free radicals. [40] Moreover, the introduced PN led to a higher PDS depletion

(Figure 3d), suggesting that the organic pollutants can rapidly scavenge the generated $^1O_2$ and accelerate PDS decomposition. This is also different from the surface radical-based oxidation where the persulfate depletion would be restrained with more participation of organics and the competitive reaction with the surface active sites between organics and oxyanion. [41] Figure 3d depicts that azide and FFA yielded a higher efficiency than phenol for catalytic PDS decomposition with β-MnO_2, possibly due to their higher reaction rates towards $^1O_2$. A previous study indicated that azide or FFA is a reducing agent which may react with PMS and cannot verify the quenching effect toward $^1O_2$. [42, 43] Figure 3d shows that PDS cannot be directly decomposed by azide or FFA (1 mM), suggesting that the reactivity of PDS towards the quenching agents was low. Thus, the inhibition of phenol degradation originated from $^1O_2$ quenching by azide or FFA.

EPR technique was applied to *in situ* capture the ROS generated from β-MnO_2/PDS system using DMPO as a spin trapping agent. Not surprisingly, neither DMPO-OH nor DMPO-SO_4 was discovered. Instead, the characteristic peaks (Figure S12) with the hyperfine splittings of 1:2:1:2:1:2:1, were assigned to 5,5-dimethyl-1-pyrrolidone-2-oxyl (DMPOX, α_N = 7.3 G, α_H = 3.9 G), as a resulting product from DMPO direct oxidation by $^1O_2$. [44, 45] Besides, TEMP was a specific spin trapping agent for identification of $^1O_2$. The intense three-line signals (1:1:1) of TEMPN adducts (Figure 4, α= 16.9 G) by $^1O_2$ oxidation was observed, which was another solid evidence of $^1O_2$ generation. The addition of FFA (1 mM) would decrease the intensity of TEMPN signals (Figure 4) due to the consumption of $^1O_2$. Moreover, a methylene blue (MB)/irradiation system was employed as a reference to identify the $^1O_2$ generation. The intermediate distributions during BPA oxidation was analyzed for both MnO_2/PDS and MB/irradiation. The LC-MS results in Figure S13 demonstrated that the intermediate

products in the MnO_2/PDS system were almost the same as the singlet oxygen based system (MB/irradiation), indicating that the $^1O_2$ was produced and serves as the primary ROS in MnO_2/PDS system. The details of intermediate products are listed in Table S2.

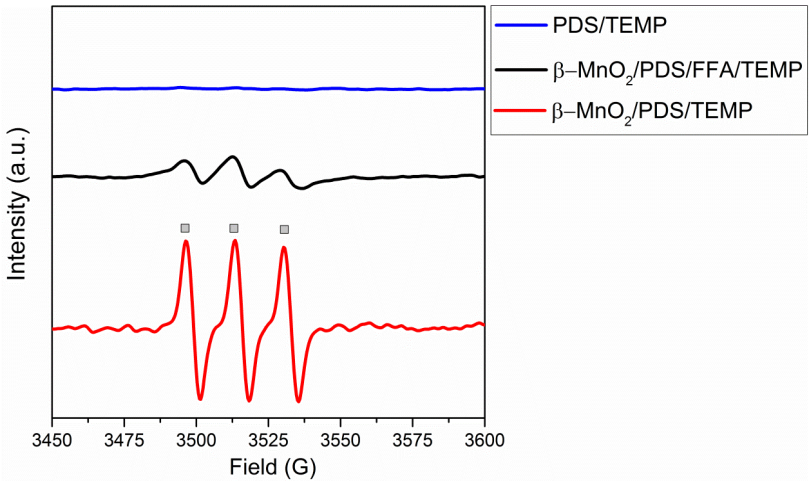

Figure 4. EPR spectra of singlet oxygen detection in the presence of TEMP. $[\beta\text{-}MnO_2]_0 = 400$ mg/L, $[PDS]_0 = 4$ mM, $[FFA]_0 = 100$ μM, $[TEMP]_0 = 25$ mM, pH buffered around 6.5, gray square: TMPO adducts.

Mechanism of singlet oxygen evolution. The impacts of solution pH and reaction substrates were investigated on $^1O_2$ generation from β-MnO_2/PDS. In Figure 5a, phenol degradation rates were significantly improved by decreasing the buffered pH from 10 to 5. At pHs 5 and 6.5, complete phenol oxidation can be achieved in 45 and 120 min, respectively, whereas only 38.1% and 31.5% of organic removals were yielded at pHs 8.5 and 10 in 180 min, respectively. Intriguingly, only 57.9% of phenol was oxidized at a lower pH of 4. At the extreme low pH region (≤ 4), significant Mn dissolution (Figure S2) was experienced and the leached Mn^{2+} is inactive for PDS activation. Moreover, surface structure of MnO_2 was destroyed, which would decrease the catalytic performance. Since the zero potential point of crystal MnO_2 was around 3.5, [46, 47] a higher pH (8.5 - 10) would cause phenomenal

electrostatic repulsions between the MnO_2 surface and persulfate anions, herein slowing down the reaction rates (Figure S14). Nevertheless, though $^1O_2$ favored to react with phenolic anions at the alkaline condition, [48] the immense repulsive forces hindered the interactions between MnO_2 and PDS and significantly prohibited the $^1O_2$ generation. Moreover, the pH effects in MnO_2/PDS manifested a completely different trend from MB/irradiation system (Figure S15), suggesting that the $^1O_2$ generation rate exerted a more significant contribution to the phenol oxidation in MnO_2/PDS, regardless of the existent forms of phenolics in the near-neutral conditions. Therefore, a neutral pH solution was more favorable.

We employed an F factor ($F = K_w/[H]^+ + K_a$, where K_a is the ionization constant of PDS at 5.5×10^{-10}) to estimate the impact of solution pH. A positive linearity between the F values and peroxide activation indicates that the reaction is pH-dependent and dominated by the persulfate ionization or base activation. [30] In this study, the nonlinear correlation between phenol degradation rate and F (Figure 5b) suggested that the reaction under neutral condition followed a heterogeneously catalytic process, whereas surface electrostatic charge may gradually impede the reaction under extreme pH conditions. [49] Nevertheless, base activation of PDS (Figure S16) may take place at high pH to generate a minor amount of hydroxyl radicals. However, the radical was less effective than the $^1O_2$-based oxidation because the electron-rich phenolic compounds were more susceptible to $^1O_2$. [31, 50]

Additionally, different solvents were applied to confirm the existence of $^1O_2$. The lifetime of $^1O_2$ in D_2O (20 - 32 μs) was more than 10-fold longer than in H_2O (2 μs), [51] which can kinetically accelerate the oxidation in $^1O_2$ based systems. [34, 42] In this study, when the solvent H_2O was completely replaced with D_2O, the phenol degradation by β-MnO_2/PDS was barely impacted at pH 10 (Figure 5c),

indicating that $^1O_2$ was not the dominant ROS under alkaline condition. However, 50% enhancement of the first order rate in phenol removal was observed at pH 6.5 in D_2O (Figure 5c, inset) compared with that in H_2O. This suggested that singlet oxygen was generated and accounted for organic degradation at the neutral pH. This is further confirmed by the EPR spectra that the intensity of TEMPN adducts in β-MnO_2/PDS/D_2O was increased obviously by 30% compared with that in β-MnO_2/PDS/H_2O at pH 6.5 as shown in Figure 5d.

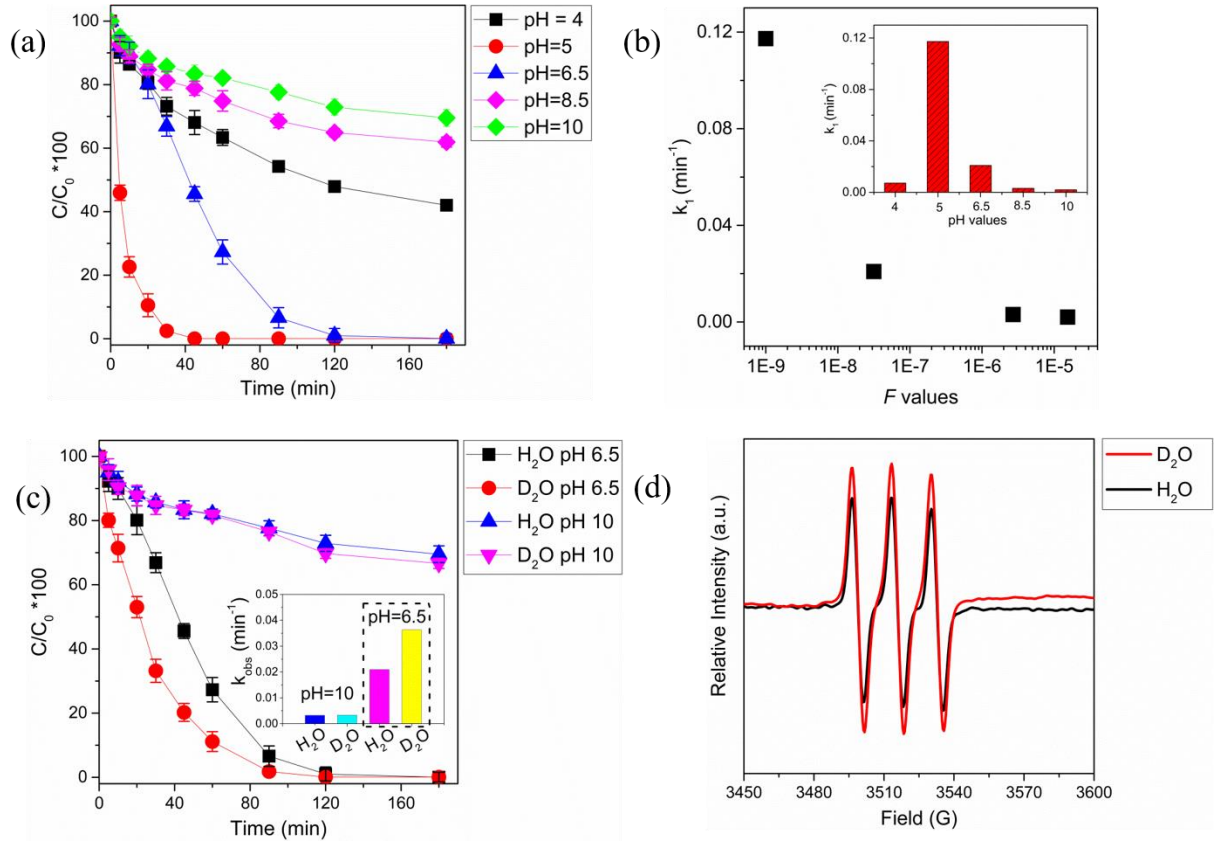

Figure 5. The insightful identification of singlet oxygen generation in β-MnO_2/PDS. (a) Phenol oxidation degradation in β-MnO_2 /PDS under different buffered pH conditions, (b) the relation of F values and degradation rates at different pH values, (c) the effect of reaction solvents (H_2O and D_2O) upon degradation, (d) EPR spectra of β-MnO_2 /PDS in the H_2O and D_2O solvents ($[TEMP]_0 = 25$ mM).

309 [β-MnO_2]$_0$ = 400 mg/L, [PDS]$_0$ = 4 mM, [phenol]$_0$ = 100 μM. 1 mM acetate buffered for pH 5, 1 mM
310 borate buffered for pH 6.5 or 8.5, and 1 mM bicarbonate buffered for pH 10.
311
312 Typically, singlet oxygen can be generated from several pathways such as the reaction between
313 persulfate (PMS/PDS) and ketonic groups on carbonaceous materials, [52] photo-excitation of oxygen
314 molecules (in a triplet ground state) via an energy-transfer process. [28] In this study, the $^1O_2$ generation
315 may be resulted from the direct oxidation or recombination of superoxide intermediates ($O_2^{\bullet-}$), which
316 could be generated over manganese dioxide. [5, 7, 9, 10] The production and role of $O_2^{\bullet-}$ can be confirmed
317 by selective scavengers of carbonate (CO_3^{2-}, $k_2 = 5 \times 10^8$ M^{-1} s^{-1}). [53] Due to the fact that
318 hydroxyl radical was not produced in this system, a high reaction rate of carbonate towards
319 hydroxyl radical ($k_2 = 3 \times 10^8$ M^{-1} s^{-1}) would not influence the inhibitory effect of $O_2^{\bullet-}$. In Figure 6,
320 addition of 1 mM carbonate decreased the phenol degradation from 100% (control experiment) to 52.5%
321 in β-MnO_2/PDS system. Only 18.8% and 17.6% phenol removals were observed when 10 and 50 mM
322 of carbonate were introduced, respectively. Besides, addition of 1 mM BQ, another more selective
323 radical scavenger for $O_2^{\bullet-}$ (BQ, $k_2 = 2.9 \times 10^9$ M^{-1} s^{-1}) [54] also impressively inhibited the phenol
324 degradation with only 29.5% organic removal. The radical quenching tests affirmed that $O_2^{\bullet-}$ was
325 involved in $^1O_2$ generation and catalytic degradation. Therefore, a superoxide-based reaction pathway
326 toward $^1O_2$ evolution on MnO_2 was proposed as displayed in Eqs 1-5. A metastable manganese
327 intermediate (Mn^{IV}-O-O-SO_3) was first formed at the surface of MnO_2, and then $O_2^{\bullet-}$ was generated
328 by reacting with another $S_2O_8^{2-}$ along with the breakage of Mn^{IV}-O. [45, 55] Afterwards, $^1O_2$ was generated
329 from a direct oxidation of $O_2^{\bullet-}$ by Mn^{IV}, which is thermodynamically favored (E_0(Mn^{IV}/ Mn^{III}) = 0.95

330 V_{NHE} and $E_0(O_2^{\bullet-}/^1O_2)$= -0.34 V_{NHE}) or a recombination of two superoxide radicals. The details were

331 shown in SI (Text S7). The similar processes were also reported in a periodate oxide/base system. [27]

332 Moreover, the specific pathway of $^1O_2$ generation by surface reactions may lead to different $^1O_2$

333 generation rates. On one hand, the competitive adsorption of different organics may result in the

334 different $^1O_2$ generation rates. On the other hand, the degradation rate can be also impacted by the

335 migration distance of $^1O_2$ as well as the ionized potential of the organics (the reactivity toward $^1O_2$). [56]

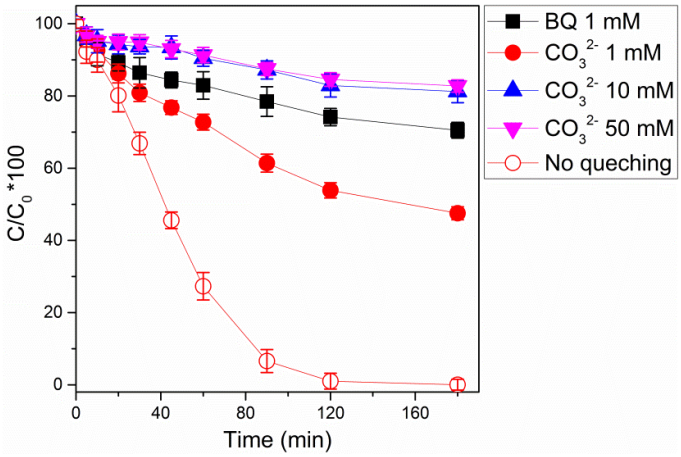

336

337 **Figure 6.** The determination of superoxide radicals by efficient scavengers. $[\beta\text{-}MnO_2]_0$ = 400 mg/L,

338 $[PDS]_0$ = 4 mM, $[phenol]_0$ = 100 μM, [BQ] = 1 mM, $[CO_3^{2-}]$ = 1 – 50 mM, pH buffered around 6.5.

339 $2[\equiv Mn(IV)\text{-}OH]^{III} + HS_2O_8^- \rightarrow 2\,[\equiv Mn(IV)\text{-}O\text{-}O\text{-}SO_3]^{II} + 3H^+$ k_1 (1)

340 $2[\equiv Mn(IV)\text{-}O\text{-}O\text{-}SO_3]^{II} + 4\,H_2O + S_2O_8^{2-} \rightarrow 2[\equiv Mn(III)\text{-}OH]^{II} + 4SO_4^{2-} + 2O_2^{\bullet-} + 8H^+$ k_2 (2)

341 $[\equiv Mn(IV)\text{-}O\text{-}O\text{-}SO_3]^{II} + O_2^{\bullet-} + OH^- \rightarrow [\equiv Mn(III)\text{-}OH]^{II} + SO_4^{2-} + {}^1O_2$ k_3 (3)

342 $2O_2^{\bullet-} + 2H_2O \rightarrow {}^1O_2 + H_2O_2 + 2OH^-$ k_4 (4)

343 $(\equiv Mn^{III}\text{-}O\text{-}O\text{-}SO_3 + H_2O \rightarrow \equiv Mn^{IV}\text{-}OH + SO_4^{\bullet-} + OH^-$

344 $S_2O_8^{2-} + O_2^{\bullet-} \rightarrow SO_4^{2-} + SO_4^{\bullet-} + O_2$

345 $SO_4^{\bullet-} + SO_4^{\bullet-} = S_2O_8^{2-})$

346 $^1O_2$ + Org. → $Org._{OX}$ k_5 (5)

The surface properties of β-MnO_2 were analyzed before and after the catalytic reaction. From the deconvolution peaks of Mn $2p_{3/2}$ in XPS spectrum (Figure S17a), the peaks of binding energies at 643.2 and 642.4 eV were assigned to Mn^{IV} and the peak at 641.3 eV corresponds to Mn^{III} species. [57] Compared to fresh MnO_2, the peak of Mn^{III} species was enhanced obviously after the reaction. The two fitted peaks of O 1s at 530.3 and 532.0 eV (Figure S17b) can be assigned to the classical Mn-O-Mn bonds and Mn-O-X bond, respectively. The intensity of Mn-O-X bond was also enhanced in the used catalyst due to the formation of metastable oxygen-containing bonds. Therefore, the alteration of surface redox states of manganese supported the proposed mechanism with the involvement of Mn^{III} intermediates, which was in agreement with FTIR and Raman analyses in Figures S18 and S19.

The corresponding kinetics (Eqs. 6-8) was established for the proposed mechanism and pseudo first-order model was calculated. The influences of single variable such as PDS and β-MnO_2 concentrations on phenol degradation at pH 6.5 (Figure S20) displayed that a higher loading of PDS or catalyst would enhance the phenol oxidation. Then, the curves between the $\ln(K_{1,obs})$ and initial PDS and MnO_2 concentrations were plotted and fitted. The good linear correlations between $\ln(K_{1,obs})$ and $\ln([MnO_2])$ (R^2 = 0.964) or ln ([PDS]) (R^2 = 0.939) were observed in the insets of Figure S21. The slopes of $\ln(K_{1,obs})$ with $\ln([MnO_2])$ and ln ([PDS]) were estimated to be 0.989 and 1.001 accordingly, suggesting that the kinetic orders were both equal to 1. The first order of $[MnO_2]$ and [PDS] could be assigned to the reactions, Eq1 and Eq2, respectively. Due to the initial amount of persulfate at an excessive level and the effect of [PDS] is neglecting, reaction rate in reaction 1 only depended on the $[MnO_2]$, which could be considered as a pseudo first-order reaction. Thus, reaction 2 was entirely related to [PDS] irrespective of $[MnO_2]$. The kinetic studies suggested that the formation of metastable manganese

intermediates (reaction 1) was a catalytic process, primarily relying on MnO_2, while the final step in evolution of $^1O_2$ may be determined by the existence form of persulfate anions. Based on PDS decomposition with manganese dioxide surface with/without phenol, the reaction rates of Eqs 1 and 2 were confirmed in Text S7. We used the Langmuir–Hinshelwood model (Text S9) to identify the role of the metastable manganese intermediates. The well fitted Langmuir–Hinshelwood model curve of PDS (R^2 = 0.942, Figure S22) indicated that the surface-mediated reaction of PDS on the MnO_2 was enhanced by increasing the PDS concentration. The enhanced surface-mediated reaction by PDS was resulted from the formation of metastable manganese-PDS intermediates, which further led to $^1O_2$ generation. Furthermore, the reaction rate from $O_2^{\bullet-}$ to $^1O_2$ in Eq 3 was calculated as 1.5×10^5 M^{-1} s^{-1} (K_3), which is three-magnitude higher than the reaction rate between superoxide and phenol (5.8×10^2 M^{-1} s^{-1}). [58] This suggested that generated $O_2^{\bullet-}$ in this system was primarily consumed for $^1O_2$ generation rather than direct contributing to phenol degradation. Moreover, based the singlet oxygen-mediated degradation of FFA, we can calculate the amount of generated $^1O_2$ by the equation of $[^1O_2] = k_{obs} / k_{FFA}$. The calculated amount of $^1O_2$ in MnO_2/PDS was 1.65×10^{-11} M (FFA 0.3 mM), which is much higher than the amount in the typical $^1O_2$-based system of Rose Bengal/irradiation (FFA 0.27 mM, 0.05×10^{-11} M). [59]

The simplified kinetic models were proposed as follows:

$$-\frac{d[organic]}{dt} = k\,[organic]_0 \quad (6)$$

$$\ln\left(\frac{[organics]_t}{[organics]_0}\right) = -K_{1,obs}t = -C k_1 K_2 K_3 (\text{or } K_4) K_5\,[MnO_2]^{n1}\,[PDS]^{n2}\,t \quad (7)$$

For apparent first-order rate constant,

$$K_{obs} = C\,K_1 K_2 K_3 (\text{or } K_4) K_5\,[MnO_2]^{n1}\,[PDS]^{n2} \quad (8)$$

where $[organics]_0$ is the initial concentration of the organic substrate, $[MnO_2]$ is the MnO_2 concentration, [PDS] is the total persulfate anions ($[HS_2O_8^-] + [S_2O_8^{2-}]$), C is the reaction constant, k_1 represents the rate of forming metastable manganese intermediate, K_2 represents the rate of forming superoxide, K_3 represents the rate of direct oxidation of superoxide for $^1O_2$ generation, K_4 represents the rate of recombination of superoxide for $^1O_2$ generation, and K_5 represents the rate of organics degradation by $^1O_2$.

Environmental Implication

In summary, we performed a comprehensive study to investigate PDS activation on manganese oxide families. Among the Mn_xO_y with distinct crystal orientations and redox states, α- and β-MnO_2 exhibited the best catalytic performance for PDS decomposition and organic degradation. Singlet oxygen was unveiled be to the primary reactive oxygen species, which exhibited a specific selectivity to the organic substances due to the mild redox potential and unique oxidation pathway. The evolution of $^1O_2$ at neutral pH was evidenced by multiple approaches such as chemical probes, quenching agents, EPR capture, and solvent exchange. In the proposed mechanism, $^1O_2$ was generated from a direct oxidation or recombination of superoxide ion radicals, and the formation of metastable manganese intermediates was identified as the key step. The hypothesis was supported by the altered manganese states after reaction and the kinetic analysis. The understanding of PDS activation by manganese oxides will be of scientific significance in manganese based ISCO and practical wastewater remediation. Firstly, the study enables the first mechanistic insights into PDS activation on manganese oxides. The catalytically active phases of MnO_2 were identified, which may contribute to the understanding of ISCO by manganese based minerals or sediment with the low-cost and chemically

stable PDS for practical remediation of contaminated soils and underground water. Secondly, apart from the classic sulfate radical based AOPs (SR-AOPs), a novel oxidative system of $^1O_2$ was identified in MnO_2/PDS system, which can be utilized for selective removal of trace organic contaminants in complicated wastewater matrix.

ASSOCIATED CONTENT

Supporting Information

The details of preparation and characterization of manganese oxides. The methods of HPLC, EPR detection, and determination of PDS concentration. Analysis of XRD patterns. The methods of LC-MS. Results of phenol removal by manganese oxides alone and Mn leaching. The phenol degradation rates by different manganese oxides. Crystal structures of Mn_2O_3 and Mn_3O_4. TEM and N_2 adsorption/desorption results. The degradation rates of different organics. Results of quenching effect. The first order kinetic of FFA decay. PDS decomposition by β-MnO_2, phenol, and β-MnO_2/phenol. EPR results by DMPO. The phenol removal by PDS alone upon different pH values. XPS spectrum results. FTIR and Raman results. The kinetic model of overall reactions.

AUTHOR INFORMATION

Corresponding Author

*Xiaoguang Duan, E-mail: xiaoguang.duan@adelaide.edu.au, School of Chemical Engineering, The University of Adelaide, Adelaide, SA 5005, Australia.

*Shaobin Wang, E-mail: shaobin.wang@adelaide.edu.au, School of Chemical Engineering, The University of Adelaide, Adelaide, SA 5005, Australia.

Notes

The authors declare no competing financial interest.

ACKNOWLEDGEMENT

Financial support from an ARC Discover project is acknowledged under project No. DP170104264. X. D. and S. W. also appreciate the partial support from Open Research Projects of State Key Laboratory (SKL-ChE-16C05 and QAK201808).

References

1. Anipsitakis, G. P.; Dionysiou, D. D.; Gonzalez, M. A. Cobalt-mediated activation of peroxymonosulfate and sulfate radical attack on phenolic compounds. Implications of chloride ions. *Environ. Sci. Technol.* **2006,** *40*, 1000-1007.

2. Anipsitakis, G. P.; Dionysiou, D. D. Radical generation by the interaction of transition metals with common oxidants. *Environ. Sci. Technol.* **2004,** *38*, 3705-3712.

3. Anipsitakis, G. P.; Dionysiou, D. D. Degradation of organic contaminants in water with sulfate radicals generated by the conjunction of peroxymonosulfate with cobalt. *Environ. Sci. Technol.* **2003,** *37*, 4790-4797.

4. Zhang, T.; Chen, Y.; Wang, Y.; Le Roux, J.; Yang, Y.; Croué, J.-P. Efficient peroxydisulfate activation process not relying on sulfate radical generation for water pollutant degradation. *Environ. Sci. Technol.* **2014,** *48*, 5868-5875.

5. Fang, G. D.; Dionysiou, D. D.; Al-Abed, S. R.; Zhou, D.-M. Superoxide radical driving the activation of persulfate by magnetite nanoparticles: implications for the degradation of PCBs. *Appl. Catal., B* **2013,** *129*, 325-332.

6. Fang, G.; Wu, W.; Liu, C.; Dionysiou, D. D.; Deng, Y.; Zhou, D. Activation of persulfate with vanadium species for PCBs degradation: A mechanistic study. *Appl. Catal., B* **2017,** *202*, 1-11.

7. Lin, K.; Liu, W.; Gan, J. Oxidative removal of bisphenol A by manganese dioxide: efficacy, products, and pathways. *Environ. Sci. Technol.* **2009,** *43*, 3860-3864.

8. Chen, W. R.; Ding, Y.; Johnston, C. T.; Teppen, B. J.; Boyd, S. A.; Li, H. Reaction of lincosamide antibiotics with manganese oxide in aqueous solution. *Environ. Sci. Technol.* **2010,** *44*, 4486-4492.

9. Furman, O.; Laine, D. F.; Blumenfeld, A.; Teel, A. L.; Shimizu, K.; Cheng, I. F.; Watts, R. J. Enhanced reactivity of superoxide in water − solid matrices. *Environ. Sci. Technol.* **2009,** *43*, 1528-1533.

10. Watts, R. J.; Sarasa, J.; Loge, F. J.; Teel, A. L. Oxidative and reductive pathways in manganese-catalyzed Fenton's reactions. *J. Environ. Eng.* **2005,** *131*, 158-164.

11. Saputra, E.; Muhammad, S.; Sun, H.; Ang, H. M.; Tade, M.; Wang, S. Different crystallographic one-dimensional MnO_2 nanomaterials and their superior performance in catalytic phenol degradation. *Environ. Sci. Technol.* **2013,** *47*, 5882-5887.

12. Wang, Y.; Indrawirawan, S.; Duan, X.; Sun, H.; Ang, H. M.; Tadé, M. O.; Wang, S. New insights into heterogeneous generation and evolution processes of sulfate radicals for phenol degradation over one-dimensional α-MnO_2 nanostructures. *Chem. Eng. J.* **2015,** *266*, 12-20.

13. Liu, H.; Bruton, T. A.; Li, W.; Buren, J. V.; Prasse, C.; Doyle, F. M.; Sedlak, D. L. Oxidation of benzene by persulfate in the presence of Fe (III) - and Mn (IV) - containing oxides: stoichiometric efficiency and transformation products. *Environ. Sci. Technol.* **2016,** *50*, 890-898.

14. Liu, H.; Bruton, T. A.; Doyle, F. M.; Sedlak, D. L. In situ chemical oxidation of contaminated

473 groundwater by persulfate: decomposition by Fe (III) - and Mn (IV) - containing oxides and aquifer
474 materials. *Environ. Sci. Technol.* **2014,** *48*, 10330-10336.
475 15. Wang, L.; Jiang, J.; Pang, S.-Y.; Zhou, Y.; Li, J.; Sun, S.; Gao, Y.; Jiang, C. Oxidation of bisphenol
476 A by nonradical activation of peroxymonosulfate in the presence of amorphous manganese dioxide.
477 *Chem. Eng. J.* **2018,** *352*, 1004-1013.
478 16. Tian, N.; Tian, X.; Nie, Y.; Yang, C.; Zhou, Z.; Li, Y. Biogenic manganese oxide: an efficient
479 peroxymonosulfate activation catalyst for tetracycline and phenol degradation in water. *Chem. Eng. J.*
480 **2018,** *352*, 469-476.
481 17. Duan, X.; Sun, H.; Shao, Z.; Wang, S. Nonradical reactions in environmental remediation
482 processes: uncertainty and challenges. *Appl. Catal., B* **2017,** *224*, 973-982.
483 18. Wang, X.; Li, Y. Selected-control hydrothermal synthesis of α-and β-MnO_2 single crystal
484 nanowires. *J. Am. Chem. Soc.* **2002,** *124*, 2880-2881.
485 19. Wang, X.; Li, Y. Synthesis and formation mechanism of manganese dioxide nanowires/nanorods.
486 *Chem.-Eur. J.* **2003,** *9* (1), 300-306.
487 20. Saputra, E.; Muhammad, S.; Sun, H.; Ang, H.-M.; Tadé, M. O.; Wang, S. Manganese oxides at
488 different oxidation states for heterogeneous activation of peroxymonosulfate for phenol degradation
489 in aqueous solutions. *Appl. Catal., B* **2013,** *142*, 729-735.
490 21. Lee, H.; Lee, H.-J.; Jeong, J.; Lee, J.; Park, N.-B.; Lee, C. Activation of persulfates by carbon
491 nanotubes: Oxidation of organic compounds by nonradical mechanism. *Chem. Eng. J.* **2015,** *266*, 28-
492 33.
493 22. Han, X.; Zhang, T.; Du, J.; Cheng, F.; Chen, J. Porous calcium–manganese oxide microspheres

494 for electrocatalytic oxygen reduction with high activity. *Chem. Sci.* **2013,** *4*, 368-376.
495 23. Kim, C.; Ahn, J.-Y.; Kim, T. Y.; Shin, W. S.; Hwang, I. Activation of persulfate by nanosized zero-
496 valent iron (NZVI): Mechanisms and transformation products of NZVI. *Environ. Sci. Technol.* **2018,**
497 *52*, 3625-3633.
498 24. Neta, P.; Madhavan, V.; Zemel, H.; Fessenden, R. W. Rate constants and mechanism of reaction
499 of sulfate radical anion with aromatic compounds. *J. Am. Chem. Soc.* **1977,** *99*, 163-164.
500 25. Buxton, G. V.; Greenstock, C. L.; Helman, W. P.; Ross, A. B. Critical review of rate constants for
501 reactions of hydrated electrons, hydrogen atoms and hydroxyl radicals ($^{\cdot}OH/^{\cdot}O^{-}$ in aqueous solution.
502 *J. Phys. Chem. Ref. Data* **1988,** *17*, 513-886.
503 26. Yun, E. T.; Moon, G. H.; Lee, H.; Jeon, T. H.; Lee, C.; Choi, W.; Lee, J. Oxidation of organic
504 pollutants by peroxymonosulfate activated with low-temperature-modified nanodiamonds:
505 Understanding the reaction kinetics and mechanism. *Appl. Catal., B* **2018,** *237*, 432-441.
506 27. Bokare, A. D.; Choi, W. Singlet-oxygen generation in alkaline periodate solution. *Environ. Sci.*
507 *Technol.* **2015,** *49*, 14392-14400.
508 28. Lee, J.; Hong, S.; Mackeyev, Y.; Lee, C.; Chung, E.; Wilson, L. J.; Kim, J. H.; Alvarez, P. J.
509 Photosensitized oxidation of emerging organic pollutants by tetrakis C_{60} aminofullerene-derivatized
510 silica under visible light irradiation. *Environ. Sci. Technol.* **2011,** *45*, 10598-10604.
511 29. Hu, P.; Su, H.; Chen, Z.; Yu, C.; Li, Q.; Zhou, B.; Alvarez, P. J.; Long, M. Selective degradation
512 of organic pollutants using an efficient metal-free catalyst derived from carbonized polypyrrole via
513 peroxymonosulfate activation. *Environ. Sci. Technol.* **2017,** *51*, 11288-11296.
514 30. Zhou, Y.; Jiang, J.; Gao, Y.; Ma, J.; Pang, S. Y.; Li, J.; Lu, X. T.; Yuan, L. P. Activation of

515 peroxymonosulfate by benzoquinone: a novel nonradical oxidation process. *Environ. Sci. Technol.*
516 **2015,** *49*, 12941-12950.
517 31. Tratnyek, P. G.; Hoigne, J. Oxidation of substituted phenols in the environment: a QSAR analysis
518 of rate constants for reaction with singlet oxygen. *Environ. Sci. Technol.* **1991,** *25*, 1596-1604.
519 32. Neta, P.; Huie, R. E.; Ross, A. B. Rate constants for reactions of inorganic radicals in aqueous
520 solution. *J. Phys. Chem. Ref. Data* **1988,** *17*, 1027-1284.
521 33. Gsponer, H. E.; Previtali, C. M.; García, N. A. Kinetics of the photosensitized oxidation of
522 polychlorophenols in alkaline aqueous solution. *Toxicol Environ. Chem.* **1987,** *16*, 23-37.
523 34. Haag, W. R.; Hoigne, J. Singlet oxygen in surface waters. 3. Photochemical formation and steady-
524 state concentrations in various types of waters. *Environ. Sci. Technol.* **1986,** *20*, 341-348.
525 35. Mostafa, S. N.; Rosario-Ortiz, F. L. Singlet oxygen formation from wastewater organic matter.
526 *Environ. Sci. Technol.* **2013,** *47*, 8179-8186.
527 36. Scully Jr, F. E.; Hoigné, J. Rate constants for reactions of singlet oxygen with phenols and other
528 compounds in water. *Chemosphere*, **1987**, *16*, 681-694.
529 37. Huie, R. E.; Clifton, C. L. Temperature dependence of the rate constants for reactions of the sulfate
530 radical, SO_4^-, with anions. *J. Phys. Chem.* **1990,** *94*, 8561-8567.
531 38. Minero, C.; Mariella, G.; Maurino, V.; Vione, D.; Pelizzetti, E. Photocatalytic transformation of
532 organic compounds in the presence of inorganic ions. 2. competitive reactions of phenol and alcohols
533 on a titanium dioxide− fluoride system. *Langmuir* **2000,** *16*, 8964-8972.
534 39. Kim, H.; Kim, W.; Mackeyev, Y.; Lee, G. S.; Kim, H. J.; Tachikawa, T.; Hong, S.; Lee, S.; Kim,
535 J.; Wilson, L. J. Selective oxidative degradation of organic pollutants by singlet oxygen-mediated

536 photosensitization: tin porphyrin versus C_{60} aminofullerene systems. *Environ. Sci. Technol.* **2012,** *46*,
537 9606-9613.
538 40. Thompson, R. C. Catalytic decomposition of peroxymonosulfate in aqueous perchloric acid by
539 the dual catalysts silver (1^+) and peroxydisulfate (2^-) and by cobalt (2^+). *Inorg. Chem.* **1981,** *20*, 1005-
540 1010.
541 41. Feng, Y.; Lee, P.-H.; Wu, D.; Shih, K. Surface-bound sulfate radical-dominated degradation of 1,
542 4-dioxane by alumina-supported palladium (Pd/Al_2O_3) catalyzed peroxymonosulfate. *Water Res.* **2017,**
543 *120*, 12-21.
544 42. Yang, Y.; Banerjee, G.; Brudvig, G. W.; Kim, J.-H.; Pignatello, J. J. Oxidation of organic
545 compounds in water by unactivated peroxymonosulfate. *Environ. Sci. Technol.* **2018,** *52*, 5911-5919.
546 43. Yun, E. T.; Lee, J. H.; Kim, J.; Park, H. D.; Lee, J. Identifying the nonradical mechanism in the
547 peroxymonosulfate activation process: Singlet oxygenation versus mediated electron transfer. *Environ.*
548 *Sci. Technol.* **2018,** *52*, 7032-7042.
549 44. Bilski, P.; Reszka, K.; Bilska, M.; Chignell, C. Oxidation of the spin trap 5, 5-dimethyl-1-pyrroline
550 N-oxide by singlet oxygen in aqueous solution. *J. Am. Chem. Soc.* **1996,** *118*, 1330-1338.
551 45. Pan, X.; Chen, J.; Wu, N.; Qi, Y.; Xu, X.; Ge, J.; Wang, X.; Li, C.; Qu, R.; Sharma, V. K.
552 Degradation of aqueous 2, 4, 4′-Trihydroxybenzophenone by persulfate activated with nitrogen doped
553 carbonaceous materials and the formation of dimer products. *Water Res.* **2018,** *143*, 176-187.
554 46. Zhao, Z.; Zhao, J.; Yang, C. Efficient removal of ciprofloxacin by peroxymonosulfate/Mn_3O_4 -
555 MnO_2 catalytic oxidation system. *Chem. Eng. J.* **2017,** *327*, 481-489.
556 47. Zhang, S.; Gutierrez, L.; Niu, X. Z.; Qi, F.; Croue, J. P. The characteristics of organic matter

influence its interfacial interactions with MnO_2 and catalytic oxidation processes. *Chemosphere* **2018,** *209*, 950-959.

48. Miller, J. S. Rose bengal-sensitized photooxidation of 2-chlorophenol in water using solar simulated light. *Water Res.* **2005**, *39*, 412-422.

49. Kolthoff, I.; Miller, I. The chemistry of persulfate. I. The kinetics and mechanism of the decomposition of the persulfate ion in aqueous medium1. *J. Am. Chem. Soc.* **1951,** *73*, 3055-3059.

50. Furman, O. S.; Teel, A. L.; Watts, R. J. Mechanism of base activation of persulfate. *Environ. Sci. Technol.* **2010,** *44*, 6423-6428.

51. Gorman, A.; Rodgers, M. Singlet molecular oxygen. *Chem. Soc. Rev.* **1981,** *10*, 205-231.

52. Cheng, X.; Guo, H.; Zhang, Y.; Wu, X.; Liu, Y. Non-photochemical production of singlet oxygen via activation of persulfate by carbon nanotubes. *Water Res.* **2017**, *113*, 80-88.

53. Lin, J. M.; Arakawa, H.; Yamada, M. Flow injection chemiluminescent determination of trace amounts of hydrogen peroxide in snow-water using KIO_4–K_2CO_3 system. *Anal. Chim. Acta* **1998,** *371*, 171-176.

54. Eyer, P. Effects of superoxide dismutase on the autoxidation of 1, 4-hydroquinone. *Chem.-Biol. Interact.* **1991,** *80*, 159-176.

55. Chan, Z. M.; Kitchaev, D. A.; Weker, J. N.; Schnedermann, C.; Lim, K.; Ceder, G.; Tumas, W.; Toney, M. F.; Nocera, D. G. Electrochemical trapping of metastable Mn^{3+} ions for activation of MnO_2 oxygen evolution catalysts. *Proc. Natl. Acad. Sci.* **2018**, *115*, E5261-E5268.

56. Li, X.; Huang, X.; Xi, S.; Miao, S.; Ding, J.; Cai, W.; Liu, S.; Yang, X.; Yang, H.; Gao, J.; Wang, J.; Huang, Y.; Zhang, T.; Liu, B. Single cobalt atoms anchored on porous n-doped graphene with dual

reaction sites for efficient Fenton-like catalysis. *J. Am. Chem. Soc.* **2018**, *140*, 12469-12475.

57. Peng, X.; Guo, Y.; Yin, Q.; Wu, J.; Zhao, J.; Wang, C.; Tao, S.; Chu, W.; Wu, C.; Xie, Y. Double-exchange effect in two-dimensional MnO_2 nanomaterials. *J. Am. Chem. Soc.* **2017,** *139*, 5242-5248.

58. Tsujimoto, Y.; Hashizume, H.; Yamazaki, M. Superoxide radical scavenging activity of phenolic compounds. *Int. J. Biochem.* **1993,** *25*, 491-494.

59. Brame, J.; Long, M.; Li, Q.; Alvarez, P. Trading oxidation power for efficiency: differential inhibition of photo-generated hydroxyl radicals versus singlet oxygen. *Water Res.* **2014**, *60*, 259-266.

585

586 **Table of Content Entry /TOC**

587

588

589

590

591

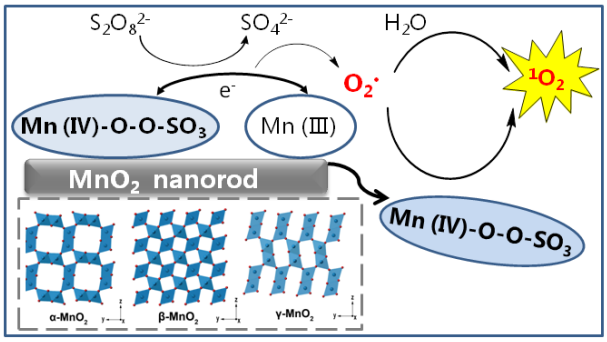

592

593

594

595

596